Origin of increased helium density inside bubbles in $Ni_{(1−x)}Fe_x$ alloys

F. Granberg [a,1,*], X. Wang [b,1,*], D. Chen [c], K. Jin [d], Y. Wang [c], H. Bei [d], W.J. Weber [e,d], Y. Zhang [d,e], K.L. More [b], K. Nordlund [a], F. Djurabekova [a,f]

[a] Department of Physics, University of Helsinki, P.O. Box 43, FIN-00014, Finland
[b] Center for Nanophase Materials Sciences, Oak Ridge National Laboratory, Oak Ridge, TN, USA
[c] Materials Science and Technology Division, Los Alamos National Laboratory, Los Alamos, NM, USA
[d] Materials Science and Technology Division, Oak Ridge National Laboratory, Oak Ridge, TN, USA
[e] Department of Materials Science and Engineering, University of Tennessee, Knoxville, TN, USA
[f] Helsinki Institute of Physics, University of Helsinki, P.O. Box 43, FIN-00014, Finland

ARTICLE INFO

ABSTRACT

Due to virtually no solubility, He atoms implanted or created inside materials tend to form bubbles, which are known to damage material properties through embrittlement. Higher He density in nano-sized bubbles was observed both experimentally and computationally in $Ni_{(100−x)}Fe_x$-alloy samples compared to Ni. The bubbles in the $Ni_{(100−x)}Fe_x$-alloys were observed to be faceted, whereas in elemental Ni they were more spherical. Molecular dynamics simulations showed that stacking fault structures formed around bubbles at maximum He density. Higher Fe concentrations stabilize stacking fault structures, suppress evolution of dislocation network around bubbles and suppress complete dislocation emission, leading to higher He density.

Due to an extremely low solubility of helium in most solid materials, He atoms, either implanted or generated due to nuclear reactions, tend to cluster and form bubbles [1]. The formation of He bubbles is mainly responsible for radiation-induced embrittlement of structural materials subject to neutron bombardment in fusion and fission reactors [2,3].

For small He-vacancy clusters in Fe, molecular dynamics (MD) simulations showed that the growth of He bubbles depends on the He-to-vacancy ratio ($r_{He/V}$), as the binding energy of He atoms, vacancies or self-interstitials to a He-vacancy cluster primarily changes with $r_{He/V}$ [4–6]. With an increasing $r_{He/V}$, the vacancy binding energy increases, whereas the binding energies of He and self-interstitials decrease, resulting in an equilibrium at $r_{He/V} \approx 1.8$ [5,6]. Golubov et al. found that small bubbles migrate mostly via surface vacancy diffusion [7]. Therefore, a higher He pressure could suppress small bubble migration, leading to lower bubble growth rates [8]. For larger He bubbles, electron energy loss spectroscopy (EELS) measurements discovered that He density

within bubbles decreases as the bubble size increases in metallic alloys [9,10], agreeing with the Young–Laplace law [7,9].

Previous studies on He bubbles revealed faceting of He bubbles, both experimentally [11–13] and computationally [14]. Ofan et al. noted in $LiNbO_3$ that a threshold radius exists, where bubbles transform from a spherical to a faceted shape [12]. This critical radius is proportional to the ratio of the bubble surface energy to the strain energy, hence also on bubble pressure as it affects the strain energy. In BCC Fe, it has been observed computationally that He bubbles form facets, as dictated by the elastic and plastic properties of Fe [14].

Despite many insights provided by previous works, few studies have focused on the effects of alloy chemistry on He bubbles. Recent studies have demonstrated that an efficient approach to improve materials radiation resistance is tuning the chemical complexity of alloys [15,16]. Specifically, He bubble growth is suppressed in NiCoCrFe when compared to Ni [17,18]. Transmission electron microscopy (TEM) analyses of $Ni_{(100−x)}Fe_x$-alloys showed that higher Fe concentrations correlate with smaller average bubble sizes and higher He densities, but the reasons for such correlations are not fully understood [19].

In this paper, we investigate the effects of Fe concentration on the resultant He densities inside bubbles by combining MD simulations and electron microscopy analyses. We find that the He

* Corresponding authors.
E-mail addresses: fredric.granberg@helsinki.fi (F. Granberg), xvw5285@psu.edu (X. Wang).
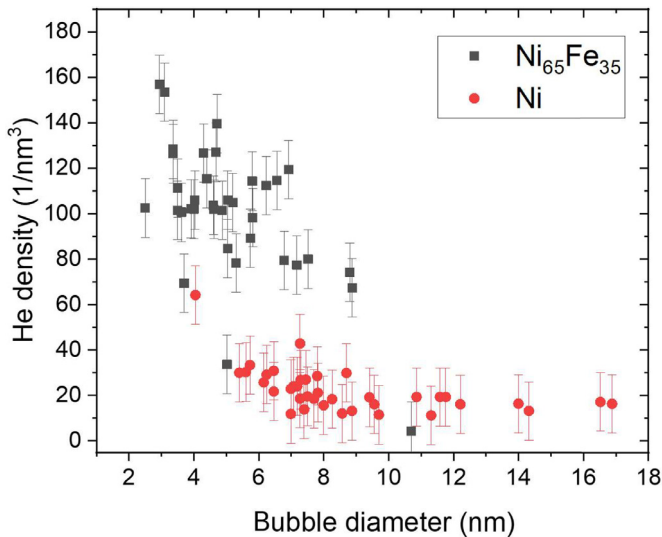[1] These authors contributed equally to this work.

Fig. 1. Experimental He density inside bubbles with different sizes in Ni and Ni$_{65}$Fe$_{35}$. The uncertainty is estimated based on energy resolution (0.45eV) of EELS signal.

densities increase with Fe concentration in Ni$_{(100−x)}$Fe$_x$-alloys and the increased He densities originated in a smaller volume expansion due to suppressed dislocation emission/formation. The mechanisms revealed here could potentially be applied to other systems and guide future alloy design for superior resistance to bubble formation. In addition, we show that bubbles in Ni$_{50}$Fe$_{50}$ maintain a more faceted shape than bubbles in Ni, correlated with observed relative surface energy differences of different alloys under pressure.

He bubbles in Ni and Ni$_{(100−x)}$Fe$_x$-alloys were studied both experimentally and computationally (x = 20 at.%, 35 at.% and 50 at.%). He densities in bubbles were measured using EELS in a scanning transmission electron microscope (STEM). The shapes of nanosized bubbles were analyzed based on high angle annular dark field (HAADF)-STEM images. Computationally differently sized He bubbles of different densities were relaxed utilizing MD simulation for the different alloys to obtain the relaxed structures and bubble sizes. All details on alloy fabrication, He irradiation, microscopy characterization and simulation methodology can be found in the Supplementary material.

Before measuring He densities using EELS, the bubble size distribution in Ni and Ni$_{65}$Fe$_{35}$ were compared using TEM images. As shown in Supplementary Figs. S3 and S4, the average bubble size in Ni$_{65}$Fe$_{35}$ is smaller than Ni, demonstrating that bubble growth is suppressed by the higher Fe concentration. EELS-measured He densities inside bubbles as a function of bubble diameter are summarized in Fig. 1. Two trends can be identified. First, for bubbles in the same material, the He density decreases as the bubble size increases. Similar trends are reported in martensitic steels and Pd$_{90}$Pt$_{10}$-alloys, which agree with the Young-Laplace law, suggesting the matrix around the bubbles is elastically deformed [9,10]. Second, for bubbles of similar sizes, the He density increases as the Fe concentration increases. For example, for bubbles between 4-7nm, the average He density in Ni is 35±27 nm$^{−3}$, whereas the average He density in Ni$_{65}$Fe$_{35}$ is 105±24 nm$^{−3}$. As mentioned earlier, an increased He density inside bubbles could stabilize He-vacancy clusters, contributing to suppressing cluster coalescence and bubble growth.

In addition, differences in bubble shape can be clearly observed between Ni and Ni$_{(100−x)}$Fe$_x$-alloys. The atomic-resolution HAADF-STEM images in Fig. 2(a) were acquired from Ni and Ni$_{50}$Fe$_{50}$ with

the samples tilted to the [110] zone axis. According to these images, bubbles in Ni$_{50}$Fe$_{50}$ exhibit obvious faceting. Viewing along [110], bubbles exhibit a hexagonal shape with the edges parallel to (100) and (111) planes (lower image in Fig. 2(a)). By contrast, bubbles in Ni maintain a more spherical shape, although some faceting parallel to the (100) plane can be identified (upper image in Fig. 2(a)).

In Fig. 3, the simulated evolution of the He density in the fully relaxed bubbles (upper row) and the corresponding changes in the bubble radii (lower row) are plotted as a function of $r_{He/V}$ for two different bubble sizes, the other ones are found in the Supplementary Fig. S5. Initially, both the He density and the bubble radius grow linearly with $r_{He/V}$. This linearity changes gradually to sublinear behavior for the He density until it reaches the maximum value. In the evolution of the bubble radii we observe a clear step-discontinuity, after which the growth continues nearly linear, but with a different slope (lower row of Fig. 3). Each discontinuity represents a yield of some sort, since the growth rate of the bubble size after the yield also changes. Since the He density is directly related to the gas pressure in the bubble, the sublinear growth of this parameter, before it reaches the maximal value, indicates that the surface of the bubble is yielding, slightly releasing the gas pressure in the bubble.

To understand the reason for the significant release of the accumulated pressure (drop in the He density), we turn to atomic images of the dislocation structures around the bubbles near the value of $r_{He/V}$ that resulted in the highest He density. Fig. 4 shows a 4nm bubble in Ni$_{65}$Fe$_{35}$: (a) before the maximal density is reached; (b) at the highest He density; and (c) after the octahedron breaks. We see the first yielding of the bubble surface at $r_{He/V}$ = 1.75:1, which proceeds via the formation of Shockley partial dislocations, which decorate the bubble surface with stacking faults. In Fig. 3(a), this yielding is registered as a beginning of the deviation from a perfectly linear behavior of the He density and bubble radius growths. Thereafter, the bubble gradually grows in size, increasing the volume by pushing the dislocations further away. The different mechanism explains the slightly different slope for bubble growth with an increase of $r_{He/V}$. At $r_{He/V} \approx 1.875:1$ the bubble is fully enclosed in a stacking fault octahedron and the He density reaches its maximal value. The formation of a stable stacking fault octahedron with the Lomer–Cottrell stair-rod edges, explains why the pressure increases even after the surface has yielded for the first time.

Further increase of $r_{He/V}$ leads to either breaking of the Lomer–Cottrell locks, extending the existing stacking faults farther, or emission of new dislocations from the bubble surface, contributing to formation of complex dislocation networks. We can clearly correlate the collapse of the stacking fault octahedron with discontinuity in the radius-$r_{He/V}$ function and the change of its slope. The vertical dashed lines in Fig. 3 guide the eye to the coincidence of the moments of discontinuity and the drop in He density in lower and upper plots for Ni, respectively. Evolution of dislocation networks in other alloys can be found in Supplementary Figs. S7–S10. These results show that stacking faults form easier in pure Ni and in lower Fe content alloys. Note that the configuration with highest density (marked MAX) are decorated by nearly perfect stacking fault octahedra. Since the number of simulations is discrete, the exact values of $r_{He/V}$, which would result in the maximal He density, may have been missed. However, consistently it is seen that the stacking fault octahedra formed in the Ni$_{65}$Fe$_{35}$ and Ni$_{50}$Fe$_{50}$-alloys are stronger, which allow for building higher He densities inside the bubbles before the Lomer–Cottrell locks are broken, compared to Ni$_{80}$Fe$_{20}$ and Ni. In addition to the more easily formed dislocations around the bubble, simulations showed that dislocation loops could be completely emitted from the bubbles. This was found for the two larger sizes, in all materials, and is discussed in greater detail in Supplementary S10. However, the results consis-
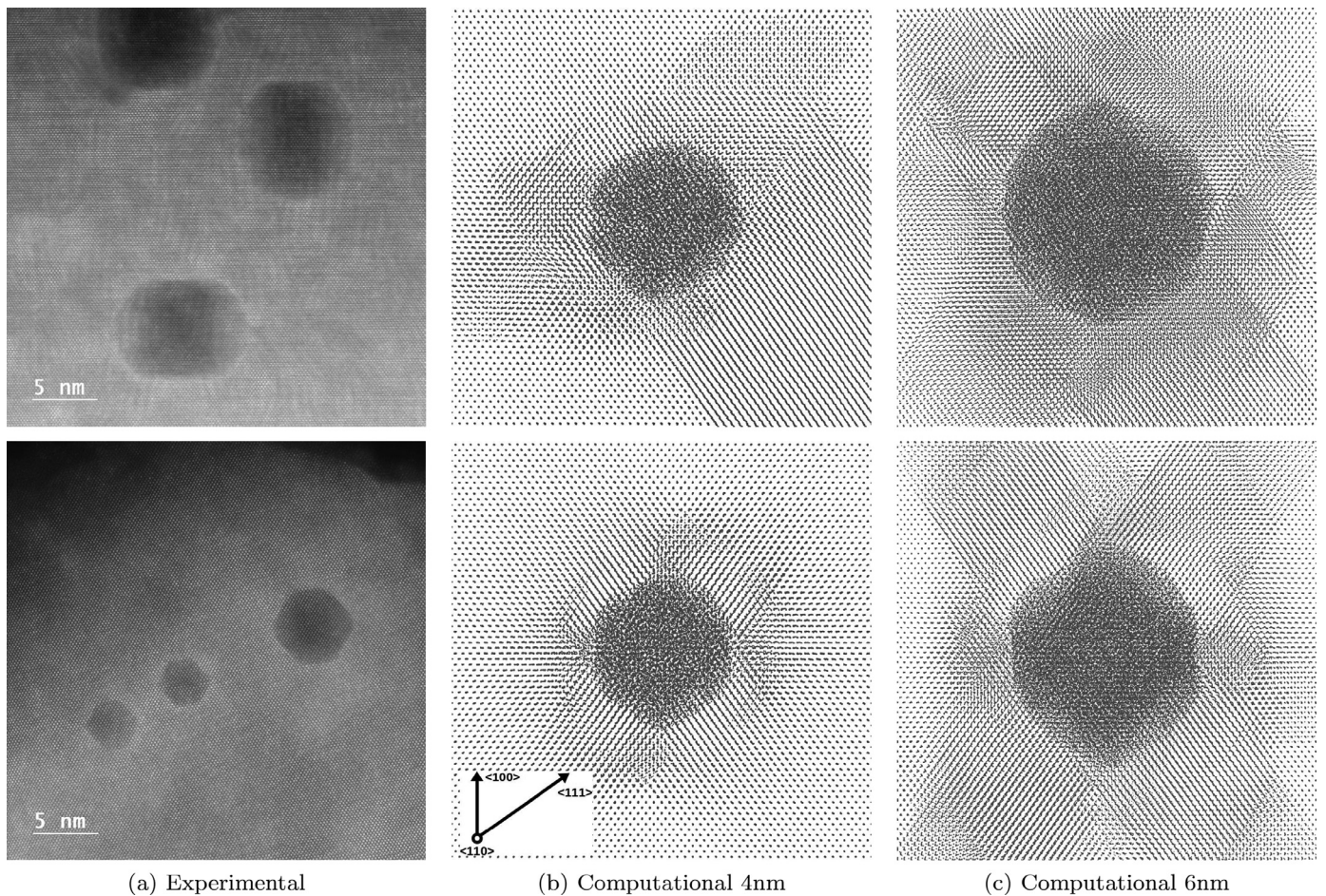
(a) Experimental   (b) Computational 4nm   (c) Computational 6nm

Fig. 2. Comparison of shape of He bubble in Ni (upper row) and $Ni_{50}Fe_{50}$ (lower row), both experimentally and computationally. The simulated cells are at a 3:1 $r_{He/V}$ for 4nm and 6nm bubbles. Directions are given in subfigure (b) lower row and are the same for all computational images.

Table 1
Maximum He density for different bubble sizes and alloys; corresponding $r_{He/V}$ at maximum density is given in parenthesis.

	2 nm	4 nm	6 nm	8 nm
Ni	147 He/nm^3 (1.875:1)	142 He/nm^3 (1.75:1)	134 He/nm^3 (1.625:1)	135 He/nm^3 (1.625:1)
$Ni_{80}Fe_{20}$	154 He/nm^3 (1.75:1)	152 He/nm^3 (2:1)	145 He/nm^3 (1.875:1)	139 He/nm^3 (1.625:1)
$Ni_{65}Fe_{35}$	157 He/nm^3 (1.875:1)	154 He/nm^3 (2:1)	147 He/nm^3 (1.875:1)	141 He/nm^3 (1.75:1)
$Ni_{50}Fe_{50}$	153 He/nm^3 (2.25:1)	153 He/nm^3 (2:1)	148 He/nm^3 (1.875:1)	142 He/nm^3 (1.75:1)

tently showed that this happened at lower $r_{He/V}$ in Ni and $Ni_{80}Fe_{20}$ than in the two alloys with higher Fe content.

Plotting the same He density as a function of the bubble diameter (Supplementary Fig. S6), we observe that bubbles grow larger in pure Ni and $Ni_{80}Fe_{20}$ than in $Ni_{65}Fe_{35}$ and $Ni_{50}Fe_{50}$ for the same $r_{He/V}$. The maximum He density reached in all cases, before the surface of the bubbles yields significantly, is consistently found at $r_{He/V} \approx 1.5$–2. The lowest maximum He density at the smallest $r_{He/V}$ is found in the bubbles in pure Ni. The maximum density and the corresponding $r_{He/V}$ is found to increase with increasing Fe concentrations in the alloys. These results are in line with the STEM-EELS density measurements, which showed the highest He density in alloys with significant Fe contents. The average maximum He concentration for all alloys and bubble sizes are shown in Table 1; the corresponding $r_{He/V}$ is also provided in parentheses.

In simulations, by rotating the cell to align with experiments, bubbles in the Fe containing alloys are more strongly faceted than those observed in elemental Ni (Fig. 2). As observed experimentally, some faceting is also observed for elemental Ni. To ex-

plain this faceting, we investigated the surface energy for free surfaces and for surfaces under pressure, found in Supplementary Tables S1–S4. They consistently show that the free (111) surfaces have the lowest energy, the free (100) surfaces have the second lowest and the free (110) and (112) surfaces have the highest energy for all alloys. Our results demonstrate three trends of gas pressure on the surface energy: (1) Addition of Fe will decrease the energy of the (100), (111) and (112) surfaces, whereas the (110) is unaffected; (2) the (111) surfaces become energetically less favorable under pressure and the surface energy is similar to that of the (100) surface; (3) the (110) surface energy is increased the most under pressure. Therefore, the end result is that the (110) surface has the highest relative surface energy, and it is the only surface clearly dependent on Fe concentration.

The maximal He density that can be retained in the bubbles is at $r_{He/V} \approx 1.8:1$ in the simulations, which is consistent with the previous results [5,6]. The maximal He density inside bubbles in pure Ni is observed at the lower values of $r_{He/V}$ compared to the Fe containing alloys, in line with the experimental results, al-
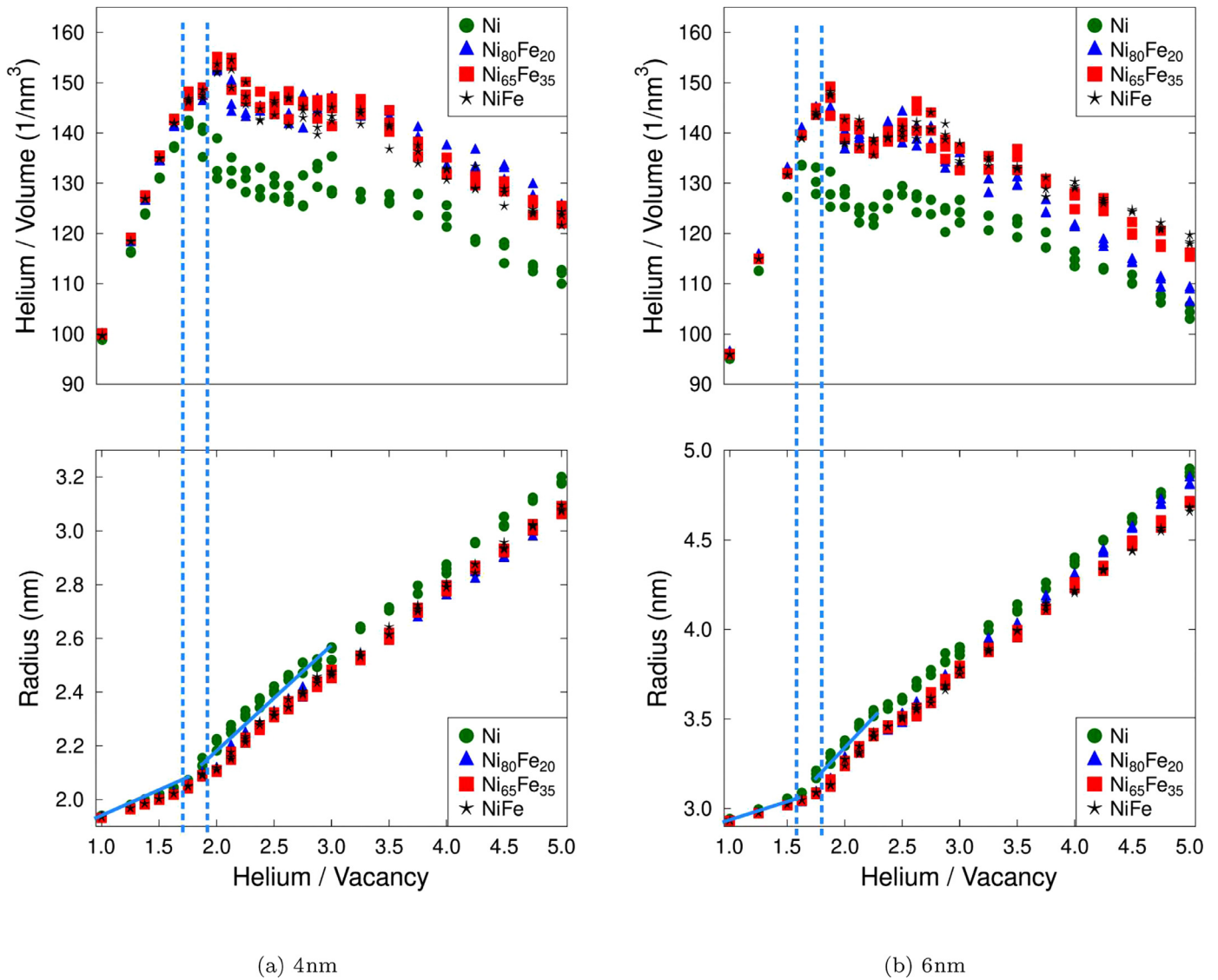
(a) 4nm

(b) 6nm

Fig. 3. He density (upper row) and bubble radius evolution (lower row) with increase of $r_{He/V}$ value in simulations for (a) 4nm and (b) 6nm bubbles. Vertical dashed lines connect and highlight locations of turning points in upper and lower graphs (for Ni). It is clear that He density stops growing when bubble surface yields, allowing for faster growth of bubble size. Solid lines in lower row guide the eye to show change of slope at turning points.
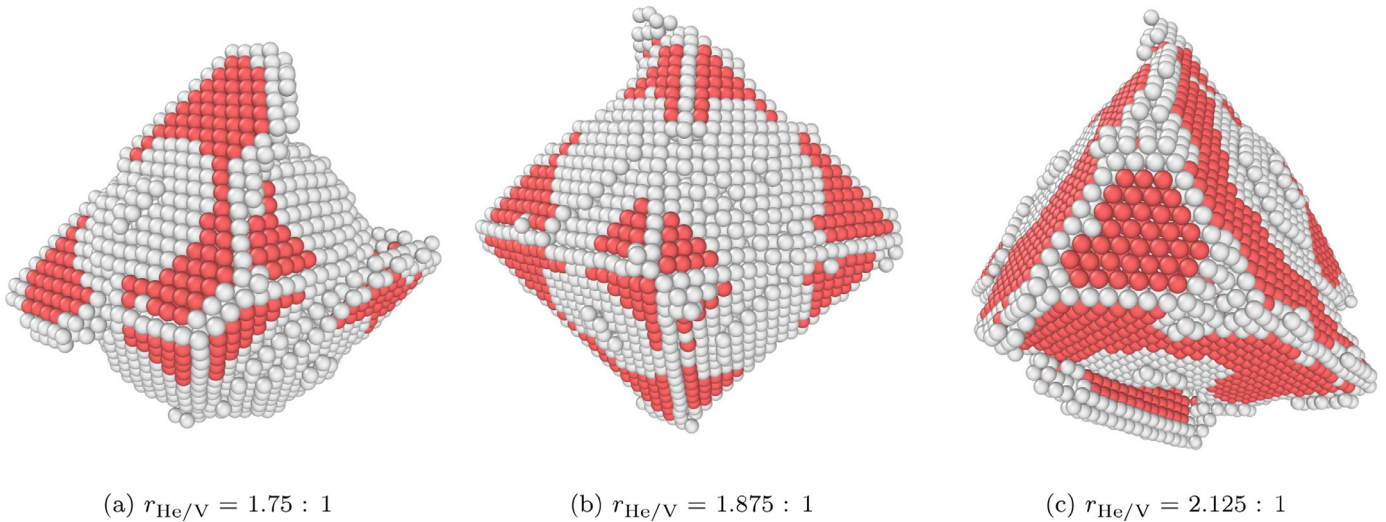

(a) $r_{He/V} = 1.75 : 1$

(b) $r_{He/V} = 1.875 : 1$

(c) $r_{He/V} = 2.125 : 1$

Fig. 4. Evolution of a 4nm He bubble at different $r_{He/V}$ for $Ni_{65}Fe_{35}$. Perfect FCC atoms are removed for visibility, red spheres corresponds to HCP lattice atoms (stacking faults) and gray spheres correspond to all other types according to aCNA. (a) First yield of surface results in some stacking faults; (b) stacking faults form a regular octahedron around bubble, which is able to hold highest He density; (c) octahedron breaks, stacking faults extend farther and other dislocations form in simulation cell.

though the differences are not as drastic as those in the STEM-EELS measurements. The general trend shown by the simulations is that the same $r_{He/V}$ induces lower He density and larger bubble volume in pure Ni compared to Fe containing alloys, where increased Fe content further increases density and suppresses bubble volume growth. Additionally, in line with experimental results, we observe that the maximal theoretical He-density decreases as the size of the bubble increases.

The detailed analysis of the atomic structure near the bubble (Supplementary Figs. S7–S10) reveals that stacking faults form easier in pure Ni and in low-Fe content alloys. We also observe the formation of regular stacking fault octahedra around the bubbles in all investigated alloys; however, in the alloys with highest Fe-concentration, this structure tends to survive for the longest time. In pure Ni, stacking fault octahedra are destroyed easier than in the alloys: a stacking fault on one side of the octahedron is able to overcome the Lomer–Cottrell lock at the edge and extends farther. Alternatively, additional dislocations are emitted from the surface of the bubble, forming more complex dislocation structures. The prolonged lifetime of the octahedron and the suppressed emission of dislocations are the reasons for the increased pressure in the bubble and the smaller bubble sizes in Ni alloys with high Fe concentrations. In addition to the more easily formed dislocations around the bubble, simulations showed that dislocation loops could be completely emitted at lower $r_{He/V}$ in Ni and $Ni_{80}Fe_{20}$ from the bubbles, which can destabilize nearby bubbles. Note that previous studies have identified other factors that may influence the He densities such as collision cascades [20–22]. A discussion regarding these factors is provided in Supplementary S11.

Previous studies showed surface energy dictate the shape of voids in Ni [23] and also plays an important role in controlling bubble shapes in BCC Fe [14]. Simulations show that there are different surface energies for different surface orientations. One surface orientation is strongly Fe-content dependent. Noteworthy is the change in order of energetically favorable surfaces when pressure is applied compared to that of free surfaces. The results show that in pure Ni, the surface energies of all four surface orientations under pressure are closer to each other than for the Fe-containing alloys. This larger relative difference in surface energies in alloys with high Fe content may lead to more faceted bubbles in the $Ni_{50}Fe_{50}$ compared to pure Ni. In addition, the faceted bubbles in $Ni_{50}Fe_{50}$ are consistent with a larger He density (and pressure) inside the bubbles in $Ni_{50}Fe_{50}$. As stated in Ref. [12], a higher bubble pressure indicates a larger bubble-induced strain energy, which can result in a smaller threshold radius for the spherical-to-faceted transition of bubbles. Therefore, the nanosized bubbles in $Ni_{50}Fe_{50}$ transform to a faceted shape while bubbles of similar size in Ni still maintain a more spherical shape.

In summary, we show by computational and experimental approaches that the maximal He density inside bubbles in $Ni_{(100-x)}Fe_x$-alloys is dependent on Fe concentration: with increasing Fe content, smaller and more pressurized He bubbles form in the alloys. The shape of the bubbles in all studied alloys evolve in a similar manner with more He atoms added to the bubble during growth. We observed that the He density in the bubble and the corresponding bubble radius initially grow linearly with an increase of the He-to-vacancy ratio. The yielding of the surface leads to a sublinear increase in the He density and a more pronounced superlinear increase in the bubble radius. Nevertheless, the most dramatic differences take place after the stacking fault octahedron formed around the bubble, by initially emitting Shockley partial dislocations, collapses. As long as the stacking fault octahedra remain intact, the He density in the bubbles increase. Increasing Fe contents in $Ni_{(100-x)}Fe_x$-alloys promotes resistance to both the formation and evolution of stacking fault octahedra, resulting in higher He densities and smaller He bubble sizes in these

alloys before yielding. Additionally, it was found that dislocation loops were completely emitted in Ni at lower $r_{He/V}$ compared to Fe-containing alloys, which could additionally destabilize nearby bubbles.

It was observed both experimentally and computationally that the He bubbles in Fe-containing alloys were more faceted than He bubbles in elemental Ni. One factor previously shown to dictate the shape of voids is the surface energy. We found that the surface energy was not only dependent on surface orientation and alloy composition, but also on the pressure exerted at the surface. Our simulations showed that the surface energies changed under pressure, as well as the relative energies of surfaces with different orientations for the same alloy composition. The most dramatic change was observed for Fe-containing alloys, consistent with faceted bubbles in these systems.

Declaration of Competing Interest

The authors declare that they have no known competing financial interests or personal relationships that could have appeared to influence the work reported in this paper.

Acknowledgments

Supplementary material

Supplementary material associated with this article can be found, in the online version, at 10.1016/j.scriptamat.2020.08.051

References

[1] H. Trinkaus, B.N. Singh, J. Nucl. Mater. 323 (2-3) (2003) 229–242.
[2] M. Samaras, Mater. Today 12 (11) (2009) 46–53.
[3] H. Trinkaus, Radiat. Effic. 101 (1–4) (1987) 91–107.
[4] G. Lucas, R. Schäublin, J. Nucl. Mater. 386 (2009) 360–362.
[5] K. Morishita, R. Sugano, B.D. Wirth, J. Nucl. Mater. 323 (2-3) (2003) 243–250.
[6] K. Morishita, R. Sugano, B.D. Wirth, T. Diaz de la Rubia, Nucl. Instrum. Methods Phys. Res. Sec. B. 202 (2003) 76–81.
[7] S.I. Golubov, R.E. Stoller, S.J. Zinkle, A.M. Ovcharenko, J. Nucl. Mater. 361 (2-3) (2007) 149–159.
[8] B.N. Singh, H. Trinkaus, J. Nucl. Mater. 186 (2) (1992) 153–165.
[9] D. Taverna, M. Kociak, O. Stéphan, A. Fabre, E. Finot, B. Décamps, C. Colliex, Phys. Rev. Lett. 100 (3) (2008) 035301.
[10] S. Fréchard, M. Walls, M. Kociak, J.P. Chevalier, J. Henry, D. Gorse, J. Nucl. Mater. 393 (1) (2009) 102–107.
[11] I.I. Chernov, A.N. Kalashnikov, B.A. Kalin, S.Y. Binyukova, J. Nucl. Mater. 323 (2) (2003) 341–345.
[12] A. Ofan, L. Zhang, O. Gaathon, S. Bakhru, H. Bakhru, Y. Zhu, D. Welch, R.M. Osgood, Phys. Rev. B 82 (2010) 104113.

[13] W.Z. Han, N.A. Mara, Y.Q. Wang, A. Misra, M.J. Demkowicz, J. Nucl. Mater. 452 (1) (2014) 57–60.

[14] S.M. Hafez-Haghighat, G. Lucas, R. Schäublin, EPL (Europhys. Lett.) 85 (6) (2009) 60008.

[15] Y. Zhang, G.M. Stocks, K. Jin, C. Lu, H. Bei, B.C. Sales, L. Wang, L.K. Béland, R.E. Stoller, G.D. Samolyuk, M. Caro, A. Caro, W.J. Weber, Nat. Commun. 6 (2015) 8736.

[16] F. Granberg, K. Nordlund, M.W. Ullah, K. Jin, C. Lu, H. Bei, L.M. Wang, F. Djurabekova, W.J. Weber, Y. Zhang, Phys. Rev. Lett. 116 (13) (2016) 135504.

[17] D. Chen, Y. Tong, H. Li, J. Wang, Y.L. Zhao, A. Hu, J.J. Kai, J. Nucl. Mater. 501 (2018) 208–216.

[18] R.W. Harrison, G. Greaves, H. Le, H. Bei, Y. Zhang, S.E. Donnelly, Curr. Opin. Solid State Mater. Sci. 23 (4) (2019) 100762.

[19] X. Wang, K. Jin, D. Chen, H. Bei, Y. Wang, W.J. Weber, Y. Zhang, K.L. More, Materialia 5 (2019) 100183.

[20] F. Wu, Y. Zhu, Q. Wu, X. Li, P. Wang, H. Wu, J. Nucl. Mater. 496 (2017) 265–273.

[21] R.E. Stoller, J. Nucl. Mater. 442 (1, Supplement 1) (2013) S674–S679.

[22] D.C. Parfitt, R.W. Grimes, J. Nucl. Mater. 381 (3) (2008) 216–222.

[23] C.W. Chen, Phys. Status Sol. (A) 16 (1) (1973) 197–210.